



HAL
open science

Numerical simulations of perforated plate liners: Analysis of the visco-thermal dissipation mechanisms

Robin Billard, Gilles Tissot, Gwénaél Gabard, Marc Versaevel

► To cite this version:

Robin Billard, Gilles Tissot, Gwénaél Gabard, Marc Versaevel. Numerical simulations of perforated plate liners: Analysis of the visco-thermal dissipation mechanisms. *Journal of the Acoustical Society of America*, 2021, 149 (1), pp.16-27. 10.1121/10.0002973 . hal-03509553

HAL Id: hal-03509553

<https://inria.hal.science/hal-03509553>

Submitted on 4 Jan 2022

HAL is a multi-disciplinary open access archive for the deposit and dissemination of scientific research documents, whether they are published or not. The documents may come from teaching and research institutions in France or abroad, or from public or private research centers.

L'archive ouverte pluridisciplinaire **HAL**, est destinée au dépôt et à la diffusion de documents scientifiques de niveau recherche, publiés ou non, émanant des établissements d'enseignement et de recherche français ou étrangers, des laboratoires publics ou privés.

Numerical Simulations of Perforated Plate Liners: Analysis of the Visco-Thermal Dissipation Mechanisms

Robin Billard, Gilles Tissot, Gwénaél Gabard, Marc Versaevel

February 4, 2020

In the linear regime and in the absence of mean flow, the impedance of perforated liners is driven by visco-thermal effects. In this paper, two numerical models are developed for predicting these visco-thermal losses. The first model is the linearized compressible Navier–Stokes equations (LNSE) solved in the frequency domain. The second model is the Helmholtz equation with a visco-thermal boundary condition accounting for the influence of the acoustic boundary layer. These models are compared and validated against measurements. The analysis of the dissipation rate due to viscosity, computed from the LNSE solutions of 4 perforated plates, highlights the presence of edges effects that are not accounted for by any models. It is also shown that a significant portion of the dissipation occurs outside the neck when considering micro perforated plates. The proposed impedance model, based on the Helmholtz equation and a visco-thermal boundary condition, is found to be computationally cheap and accurate.

1 Introduction

Perforated plate liners are widely used to reduce noise emissions from turbofans. These liners are the source of aerodynamic losses due to their surface roughness. Such friction losses can be minimized by reducing the surface roughness of the liners, which, as shown experimentally by Roberts (1977), is a function of the plate porosity and the holes diameter. Therefore, using micro perforated plates (MPP), with a porosity σ below 5 % and a neck radius R_{neck} below 0.5 mm, has become of interest to lower the flow drag of the liners.

In the linear regime without mean flow, the main dissipation mechanisms responsible for the acoustic dissipation are the visco-thermal losses. They can be described using Guess (1975) or Maa (1998) models. In addition, mathematical foundations are proposed by Laurens et al. (2013) for the Rayleigh conductivity of cylindrical perforation and unconventional apertures, such as conical and tilted perforations. In a similar modeling effort, Honzík et al. (2013) propose a transfer function derived from Zwikker and Kosten (1949) theory to model the viscous and thermal boundary layers in small horns. Joly et al. (2006) introduced a formulation of two coupled equations accounting for viscous and thermal effects in a fluid. This formulation is shown to be efficient in solving linear acoustics problems using standard numerical methods.

In the present study, two numerical models are presented and validated, with a view to investigate the acoustic losses occurring at a perforate. The first model solves the Helmholtz equation with a boundary condition accounting for the viscous and thermal acoustics boundary layers Berggren et al. (2018). This boundary condition is obtained by assuming that the rigid wall is smooth and that its radius of curvature is much greater than the viscous and thermal boundary layers thicknesses. This so-called “lossy Helmholtz” model is compared against a more detailed, but more costly, alternative model based on the linearized compressible Navier–Stokes equations (LNSE). Both models are solved in the frequency domain using finite elements. Their

results are compared against impedance tube measurements. This allows to assess the validity of the lossy Helmholtz model. Additionally, the LNSE model allows for a detailed investigation of the losses phenomenon of the micro perforated and the standard macro perforated liners ($\sigma > 5\%$, $R_{\text{neck}} > 0.5$ mm, defined in section 2). The dissipation rate per unit mass due to viscous effects is computed and the difference between micro- and macro-perforate liners are investigated.

The remainder of this paper is as follows. We first present the theoretical models in section 2. In section 3, a brief description of the numerical methods is given. A comparison between the numerical models and measurements follows in section 4 and the dissipation rate is analyzed in section 5. In section 6, the convergence of the numerical models is assessed. Finally, we conclude on the relevance of the lossy Helmholtz model in section 7.

2 Numerical models

In this section, two numerical models are described to predict the acoustic impedance of a perforated plate. The geometry of the perforated plate, which is composed of a periodic arrangement of cylindrical holes is simplified to a single hole as shown in Figure 1. The computational domain is composed of three cylindrical ducts corresponding to the exterior, the neck and the cavity of the liner. The geometry is further simplified to the 2D axi-symmetrical domain Ω showed in Figure 2.

To ensure that this non-pavable single-hole model is representative of a periodic arrangement of perforations, the Percentage Open Area (POA), also known as porosity σ , must correspond to that of the actual perforated plate. The cavity radius R_{cav} , which is equal to the exterior radius, is chosen to achieve the target plate porosity σ such that

$$\sigma = \left(\frac{R_{\text{neck}}}{R_{\text{cav}}} \right)^2 \quad (1)$$

where R_{neck} is the radius of the neck.

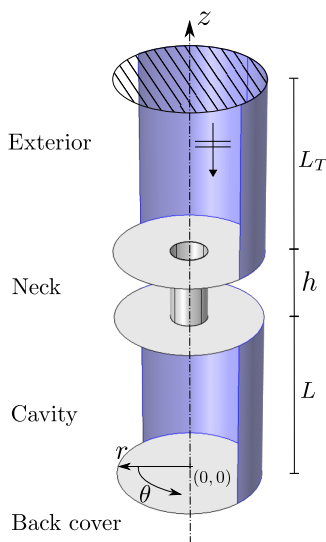


Figure 1: Schematic of the model.

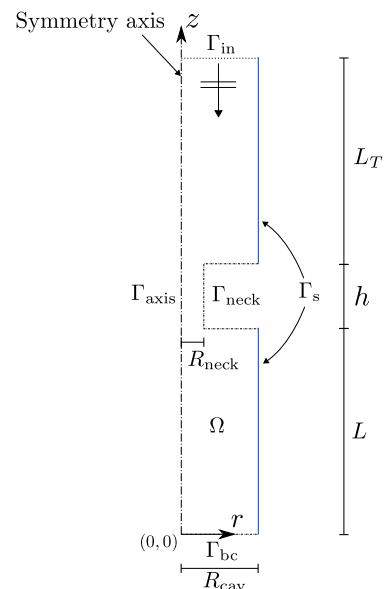


Figure 2: Axisymmetric computational domain.

On Figure 1, the blue faces are notional ducts corresponding to sliding surfaces and the grey surfaces are no-slip walls. An implicit time dependence $e^{+i\omega t}$ is used. An incoming plane wave is imposed as a boundary condition on Γ_{in} . The LNSE and the Helmholtz equation are solved in the domain Ω to calculate the reflected waves and, hence, the reflection coefficient and the effective impedance of the liner.

2.1 Linearised Navier–Stokes equations

The problem is made non-dimensional by using the following quantities: the sound speed c_0^* , the fluid density ρ_0^* and the reference length $L_{\text{ref}}^* = 2R_{\text{cav}}$ (recall that $R_{\text{cav}} = R_{\text{neck}}/\sqrt{\sigma}$). The symbol $*$ denotes dimensional quantities. It follows that variables are made non-dimensional as follows

$$x = \frac{x^*}{L_{\text{ref}}^*}, \quad \mathbf{u} = \frac{\mathbf{u}^*}{c_0^*}, \quad \rho = \frac{\rho^*}{\rho_0^*}, \quad p = \frac{p^*}{\rho_0^* c_0^{*2}}, \quad T = \frac{T^* c_p^*}{c_0^{*2}}, \quad e = \frac{e^*}{c_0^{*2}}.$$

$\mathbf{u} = (u_r, u_z)^T$ is the fluid velocity, c is the sound speed, ρ is the density, p is the pressure, T is the temperature, c_p^* is the specific heat capacity at constant pressure and e the specific internal energy. The acoustic Reynolds number and the Prandtl number are defined as follows

$$Re_a = \frac{\rho_0^* c_0^* L_{\text{ref}}^*}{\mu^*}, \quad \text{and} \quad Pr = \frac{c_p^* \mu^*}{\kappa^*}.$$

where μ^* is the dynamic viscosity and κ^* is the thermal conductivity. Both are assumed independent of temperature.

A perfect gas is assumed, which leads to the following relations between thermodynamic quantities:

$$c^2 = \gamma r T, \quad e = \frac{T}{\gamma} \quad \text{and} \quad p = \rho r T \quad \text{with} \quad r = \frac{\gamma - 1}{\gamma}.$$

$\gamma = c_p^*/c_v^*$ is the heat capacity ratio and c_v^* is the specific heat capacity at constant volume.

The equations stating the conservation of mass, momentum and energy are as follows:

$$\frac{\partial \rho}{\partial t} + \nabla \cdot (\rho \mathbf{u}) = 0, \tag{2}$$

$$\rho \frac{\partial \mathbf{u}}{\partial t} + \rho (\mathbf{u} \cdot \nabla) \mathbf{u} = -\nabla p + \nabla \cdot \boldsymbol{\tau}, \tag{3}$$

$$\frac{\rho}{\gamma} \left(\frac{\partial T}{\partial t} + \mathbf{u} \cdot \nabla T \right) = -p \nabla \cdot \mathbf{u} + \boldsymbol{\tau} : \nabla \mathbf{u} + \frac{1}{Re_a Pr} \nabla^2 T. \tag{4}$$

The viscous stress tensor $\boldsymbol{\tau}$ is given by

$$\boldsymbol{\tau} = \frac{1}{Re_a} \left[\nabla \mathbf{u} + (\nabla \mathbf{u})^T + \left(\mu_B - \frac{2}{3} \right) (\nabla \cdot \mathbf{u}) \mathbb{I} \right], \tag{5}$$

where \mathbb{I} is the identity matrix and $\mu_B = \mu_B^*/\mu^*$ is the normalized bulk viscosity.

The mass conservation equation (2), the momentum conservation equation (3) and the energy conservation equation (4) are linearized around a steady state defined by ρ_0 , \mathbf{u}_0 , p_0 and T_0 :

$$\rho = \rho_0 + \rho', \quad \mathbf{u} = \mathbf{u}_0 + \mathbf{u}', \quad p = p_0 + p', \quad T = T_0 + T',$$

in which ρ' is the perturbed density, \mathbf{u}' is the perturbed velocity, p' is the perturbed pressure and T' is the perturbed temperature. We consider a uniform quiescent medium, hence $\mathbf{u}_0 = \mathbf{0}$, $\rho_0 = 1$, $c_0 = 1$, $p_0 = 1/\gamma$ and $T_0 = 1/(\gamma-1)$. In addition we solve these equations in the frequency

domain with a $e^{+i\omega t}$ time dependence. Therefore, the linearized Navier–Stokes equations reduce to

$$i\omega\rho' + \nabla \cdot \mathbf{u}' = 0, \quad (6)$$

$$i\omega\mathbf{u}' = -\nabla p' + \frac{1}{Re_a} \nabla \cdot \left[\nabla \mathbf{u}' + (\nabla \mathbf{u}')^T + \left(\mu_B - \frac{2}{3}\right) (\nabla \cdot \mathbf{u}') \mathbb{I} \right], \quad (7)$$

$$i\omega T' = -\nabla \cdot \mathbf{u}' + \frac{\gamma}{Re_a Pr} \nabla^2 T'. \quad (8)$$

Equations (6), (7) and (8) are solved together with the following boundary conditions. An incident plane wave is defined on the upper boundary of the domain Ω :

$$\nabla p' \cdot \mathbf{n} + ikp' = 2ikWe^{+ikL_Z} \text{ on } \Gamma_{in}, \quad (9)$$

where $L_Z = L + h + L_T$ and W is the amplitude of the incoming plane wave. k is the acoustic wave number accounting for the viscosity of the fluid:

$$k = \omega \left(1 + i\omega \frac{\mu_B + \frac{4}{3}}{Re_a} \right)^{-1/2}. \quad (10)$$

See Appendix A for more detail on this.

On the perforated plate and the back cover, a no-slip condition is implemented together with an isothermal condition:

$$\mathbf{u}' = \mathbf{0}, \quad T' = 0 \text{ on } \Gamma_{neck} \text{ and } \Gamma_{bc}. \quad (11)$$

Alternatively, we will also consider the case where an adiabatic condition is imposed by setting $\nabla T' \cdot \mathbf{n} = 0$ on this surfaces.

On the sides and the axis of the domain, a free-slip boundary condition is used with an adiabatic condition:

$$\mathbf{u}' \cdot \mathbf{n} = 0, \quad \nabla T' \cdot \mathbf{n} = 0 \text{ on } \Gamma_{axis} \text{ and } \Gamma_s. \quad (12)$$

This free-slip condition is indeed representative of the interaction between perforations for a normal plane wave, due to the symmetry of the configuration.

The reflection coefficient R on the surface of the perforated plate is defined by

$$R = \left(\frac{\bar{p}}{W} - e^{ikL_T} \right) e^{ikL_T}, \quad (13)$$

where $W = 1$ and \bar{p} is the averaged pressure over the boundary Γ_{in} .

Thus, the normalized impedance at the surface of the perforated plate is determined using the following expression:

$$\frac{Z}{\rho_0 c_0} = \frac{1 + R}{1 - R}. \quad (14)$$

2.2 Helmholtz model

Inside the computational domain we solve the Helmholtz equation written for pressure:

$$\nabla^2 p + \omega^2 p = 0 \text{ in } \Omega. \quad (15)$$

As for the LNSE, an incident plane wave is defined on the upper boundary of the domain by writing

$$\nabla p \cdot \mathbf{n} + i\omega p = 2Wi e^{+i\omega L_Z} \text{ on } \Gamma_{in}. \quad (16)$$

On the axis and the sides of the domain we impose a free-slip boundary condition:

$$\nabla p \cdot \mathbf{n} = 0 \text{ on } \Gamma_{\text{axis}} \text{ and } \Gamma_{\text{s}}. \quad (17)$$

We account for the viscous and thermal boundary layers on the wall of the perforated plate and the back cover using the boundary condition developed by Berggren et al. (2018):

$$\nabla p \cdot \mathbf{n} = \delta_V \frac{i-1}{2} \nabla_T^2 p + \delta_T \omega^2 \frac{(\gamma-1)(i-1)}{2} p \text{ on } \Gamma_{\text{neck}} \text{ and } \Gamma_{\text{bc}}, \quad (18)$$

in which ∇_T^2 is the tangential Laplacian. The viscous and thermal boundary layer thicknesses are defined as follows

$$\delta_V = \sqrt{\frac{2}{\omega Re_a}} \text{ and } \delta_T = \sqrt{\frac{2}{\omega Re_a Pr}}.$$

Equation (18) is derived from the linearized compressible Navier–Stokes equations. A non-slip condition and an isothermal condition are applied on the rigid walls. The radius of curvature of the surface should also be large compared to the boundary layer thickness. Therefore, in the case of a perforate plate, this boundary condition is valid when the radius of the neck is much larger than δ_V and δ_T . This limitation is stated by Mbailassem et al. (2019) in a similar approach. Furthermore, (18) is not suitable when irregularities are present on the surface, which means this model is not expected to be valid at the corners of the hole. Another limitation is that the boundary layer should not overlap. For a perforate plate, this occurs when $\delta_V \geq R_{\text{neck}}$. Berggren et al. (2018) compared their solutions to those of Keefe (1984) for cylindrical wave guides of radius 0.1 mm and obtained good correspondence for $\delta_V/R_{\text{neck}} < 0.49$. In order to perform consistent comparisons between the numerical models and measurements, we will not consider ratio δ_V/R_{neck} above 0.49 in the following.

Finally, it is worth noting that (18) is derived using an isothermal boundary condition. If an adiabatic boundary condition was used instead, $\delta_T = 0$ is obtained.

Among the fact that a single variable is necessary for the computation, this Helmholtz model combined with (18) allows to compute rapidly the pressure field since it does not require to resolve the acoustic boundary layers. This is the key difference with the LNSE model which requires a very fine mesh to resolve the boundary layers. This is especially true for high frequencies, when the boundary layers are very thin.

3 Numerical method

The LNSE model and the Helmholtz model are both solved using the finite element method. The variational formulations are detailed in Appendices B and C. These formulations are implemented using the GetFEM++ package (Renard and Pommier, 2017) and the meshes are generated using Gmsh (Geuzaine and Remacle, 2009). Unstructured, triangular meshes are used. In the LNSE model, first order polynomials are used to interpolate the density and the temperature while second-order polynomials are used for the velocity. In the Helmholtz model, the pressure field is approximated with second-order polynomials.

| Configuration | σ (%) | R_{neck} (mm) | R_{cav} (mm) | T (mm) |
|---------------|--------------|------------------------|-----------------------|----------|
| 1 (macro) | 6.0 | 0.80 | 3.27 | 1.50 |
| 2 (macro) | 10.0 | 0.80 | 2.53 | 1.50 |
| 3 (micro) | 1.4 | 0.15 | 1.27 | 0.60 |
| 4 (micro) | 4.2 | 0.15 | 0.73 | 0.60 |

Table 1: Perforated plate configurations.

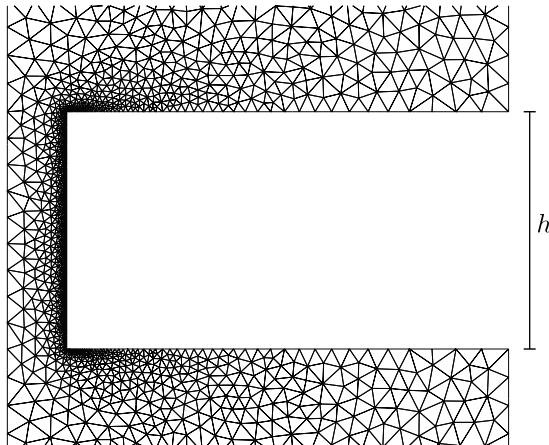


Figure 3: Example of finite element mesh for the LNSE model.

Figure 3 shows an example of finite element mesh used for the LNSE model. The mesh is refined near the neck to properly resolve the boundary layers. In addition, the corners of the neck are rounded with a radius $R_c = R_{\text{neck}}/100$ to avoid geometrical singularities. No measurable difference is observed on the predicted impedance when the computations is performed using sharp corners, but rounded corners leads to a faster mesh convergence of the numerical model.

4 Comparisons with measurements

The results obtained from the numerical models are now compared with impedance tube measurements. These measurements are carried out in accordance with the NF EN ISO 10534-2 standard method. The diameter of the tube is 29 mm. The cut-on frequency of the first non plane mode is 6932 Hz. Two 1/4" microphones with a 20 mm spacing are used to determine the surface impedance of the liners. The distance between the sample and the closest microphone is 45.2 mm. The frequency range is between 850 Hz and 3000 Hz. In order to remain in the linear regime, the Sound Pressure Level (SPL) is set to 115 dB with a white noise source. Indeed, non linear effects are already measurable on micro-perforated plates when the SPL is equal to 120 dB. The cavity height is $L = 29$ mm.

Four configurations are treated in this study to investigate the impact of the liner's geometry on the impedance. The chosen parameters are summarized in Table 1.

Configuration 1 and 2 correspond to macro-perforated plates with a low and high porosity respectively. Configuration 3 and 4 are micro-perforated plates with a low and high porosity. The neck radius is kept constant in the macro- and micro-perforated cases. In the following the normalized resistance $\text{Re}(Z)/(\rho_0 c_0)$ and the normalized plate reactance $\text{Im}(Z)/(\rho_0 c_0) + \cot(k_0 L)$ are plotted as functions of the Helmholtz number $k_0 L$, with $k_0 = \omega/c_0$.

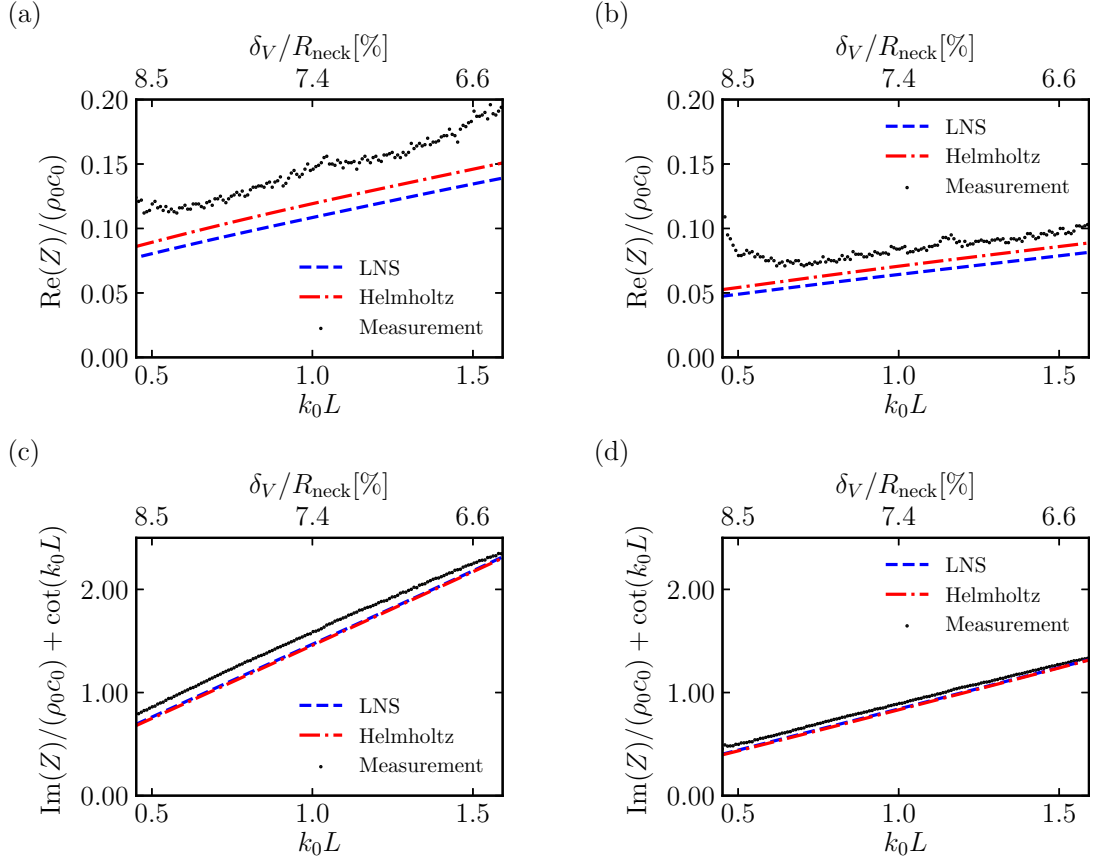


Figure 4: (a), (c) Normalized resistance and normalized plate reactance for configuration 1: a macro perforated case with a low porosity ($Re_a = 148611$, $Pr = 0.707$). (b), (d) Normalized resistance and normalized plate reactance for configuration 2: a macro perforated case with a high porosity ($Re_a = 115114$, $Pr = 0.707$).

Figure 4 shows the impedances obtained for the macro-perforated plates, for which the ratio δ_V/R_{neck} is between 9% and 5% approximately. The LNS model appears to underestimate the resistance of the macro-perforated liners. It is also the case for the Helmholtz model but to a lesser extent. However, the significance of these differences is limited since we are looking at low resistance values. As a result, the corresponding absolute error is low. The computed plate reactances present a good correspondence with the measurements.

Figure 5 shows the impedances for the micro perforated configurations, for which the ratio δ_V/R_{neck} is between 27% and 49%, which corresponds to the validity limit of the Helmholtz model. In the micro perforated case, according to Figures 5(a) and 5(b), the resistance is accurately predicted by the linearized Navier–Stokes model. The Helmholtz model also provides correct predictions of the resistance despite the fact that it is less accurate close to its validity limit (Figure 5(a)), *i.e.* when $\delta_V/R_{\text{neck}} \simeq 0.49$. Good correspondence between the measured and the modeled plate reactances is visible in Figures 5(c) and 5(d).

As mentioned in the previous section, the LNSE predictions are based on the isothermal condition on the plate and the backing plate. It is interesting to assess whether the use of an adiabatic condition would significantly change these predictions. This is shown in Figure 5(a) where the results with an adiabatic and isothermal conditions are presented side-by-side for configuration 3. Changing the nature of the thermal boundary condition only has a very limited

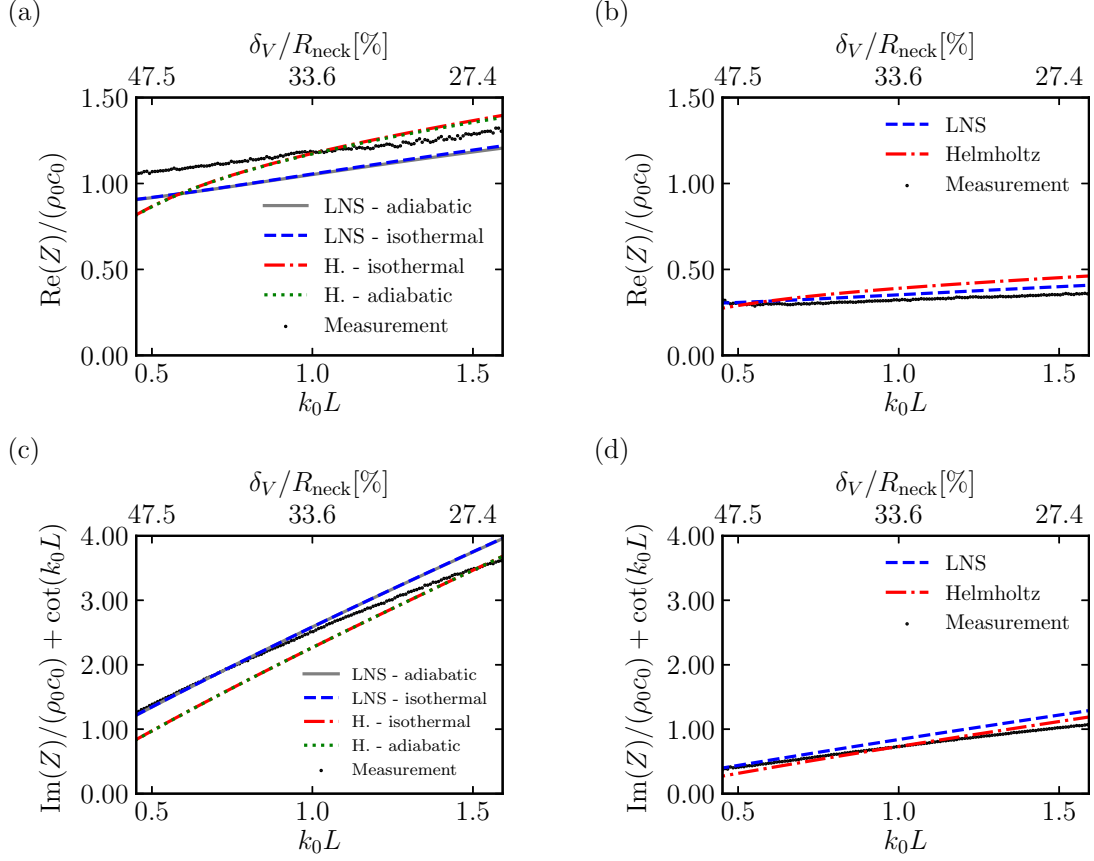


Figure 5: (a), (c) Normalized resistance and normalized plate reactance for configuration 3: a micro perforated case with a low porosity ($Re_a = 57685$, $Pr = 0.707$). (b), (d) Normalized resistance and normalized plate reactance for configuration 4: a micro perforated case with a high porosity ($Re_a = 33305$, $Pr = 0.707$).

influence on the predicted impedance.

5 Analysis of the rate of dissipation

In order to gain more insight into the dissipation mechanisms influencing the impedance of a perforated plate, we calculate the viscous dissipation rate. From equation (5), we derive its expression, separating the dissipations due to shear and bulk effects. The dissipation rate resulting from shear stresses is

$$\Phi_{\text{shear}} = \frac{1}{Re_a} \left\{ \frac{1}{2} \left[\nabla \mathbf{u} + (\nabla \mathbf{u})^T \right] : \left[\nabla \mathbf{u} + (\nabla \mathbf{u})^T \right] - \frac{2}{3} (\nabla \cdot \mathbf{u})^2 \right\}, \quad (19)$$

and the dissipation rate due to the bulk viscosity is:

$$\Phi_{\text{bulk}} = \frac{\mu_B}{Re_a} (\nabla \cdot \mathbf{u})^2. \quad (20)$$

We choose arbitrarily $\mu_B = 2/3$. In the results presented below, the integral over the whole FEM domain of the dissipation due to bulk effect Φ_{bulk} was found to be negligible compare

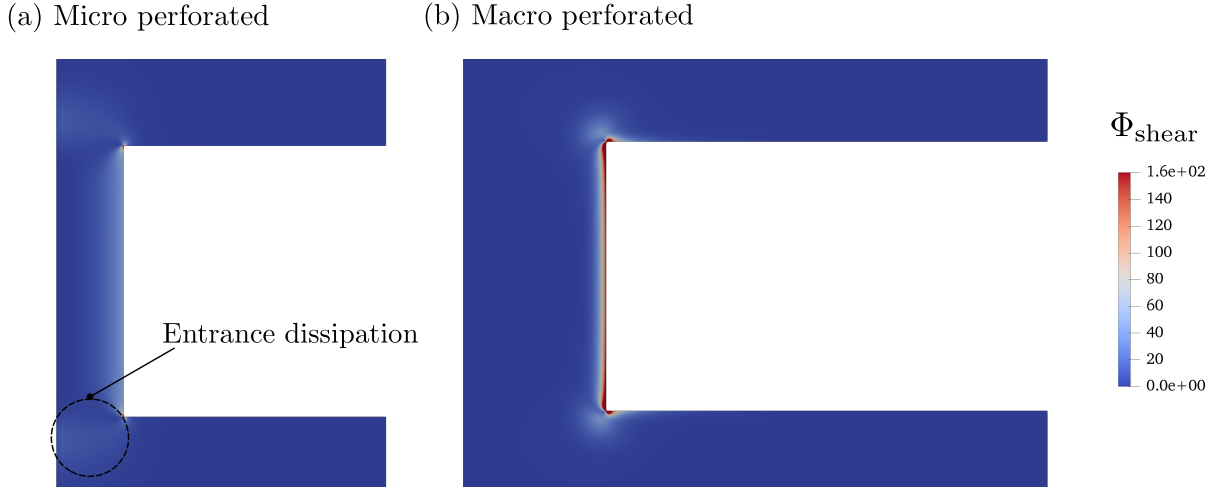


Figure 6: (a) Dissipation rate due to shear effect close the neck of micro perforated configuration 4 for $k_0L = 0.95$. (b) Dissipation rate due to shear effect close to the neck of the macro-perforated configuration 1 for $k_0L = 0.71$.

to the overall value of Φ_{shear} for all four configurations. For this reason Φ_{bulk} is not discussed further.

The dissipation rates for the micro-perforated configuration 4 and macro-perforated configuration 1 are shown in Figure 6 at their respective resonance frequencies. In both cases, an important part of the dissipation is localized in the neck. This well-known dissipation mechanism is modeled by the theory from Zwikker and Kosten (1949). In the case of a micro-perforated plate, the viscous boundary layer thickness is large compare to the neck radius, thus the dissipation is spread across the neck. In the macro-perforated configuration, for which the ratio δ_V/R_{neck} is low, the dissipation is concentrated close to the wall of the neck. In both cases, a concentration of dissipation is observed near the corners of the perforation. It is interesting to note that this is not modeled explicitly by any impedance model. Finally, viscous dissipation is also present at the entrances of the macro- and micro-perforated plaers. This is consistent with the fact that an end length is needed in the standard impedance models.

In order to qualitatively assess the differences in the distribution of dissipation rate between the micro- and macro-perforated cases, the dissipation rate due to shear effects is integrated over four domains shown in Figure 5. The domains correspond to: the exterior close to the hole entrances, the neck, the wall of the neck and the corners. The contributions from these zones is computed for the four previous configurations and compared to each others.

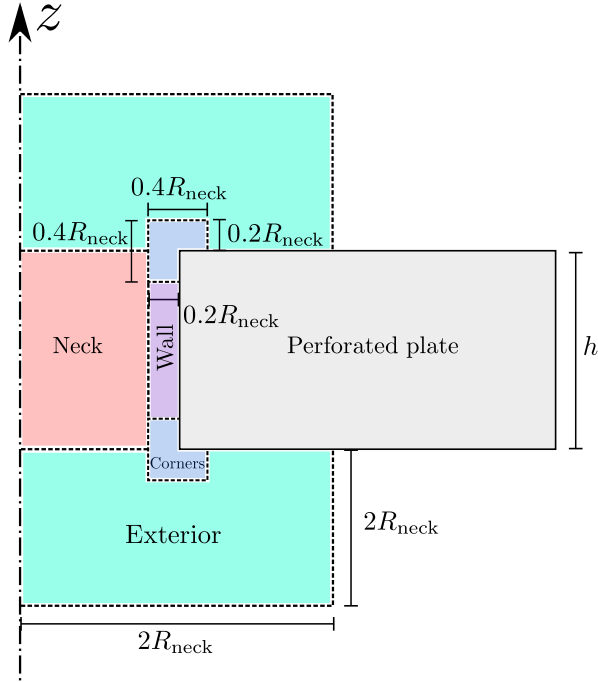


Figure 7: Schematic of the integrated surfaces.

Table 2 summarizes the contributions from each zone to the overall dissipation rate for each configuration at their respective resonance frequencies. The remaining losses in the domain do not exceed 0.6% for each configurations.

| Configuration | k_0L | δ_V/R_{neck} (%) | Exterior (%) | Corners (%) | Neck (%) | Wall(%) |
|---------------|--------|--------------------------------|--------------|-------------|----------|---------|
| 1 (macro) | 0.71 | 7.5 | 12.7 | 37.8 | 2.1 | 46.9 |
| 2 (macro) | 0.89 | 6.7 | 11.1 | 39.4 | 1.6 | 47.5 |
| 3 (micro) | 0.57 | 44.5 | 25.1 | 7.1 | 31.3 | 36.1 |
| 4 (micro) | 0.95 | 34.4 | 25.3 | 7.1 | 31.3 | 36.9 |

Table 2: Comparison of the contributions for each configuration.

The relative distribution of losses is significantly different between the macro-perforated cases 1 & 2 and the micro-perforated cases 3 & 4. In the first cases, the boundary layer thickness is small compared to the neck radius and the dissipation is localized mainly near the corners and along the neck wall. The important contribution from the corners is partly due to the fact that the ratio $h/(2R_{\text{neck}})$ is close to 1 in the macro perforated case, meaning that the corner integration zone extend far in the wall of the neck. Therefore, most of the losses occur close to the wall. This explains why, for macro-perforated configurations, the Helmholtz model with the equivalent boundary condition (18) is able to provide results similar to the LNSE model. In the micro-perforated cases, the ratio δ_V/R_{neck} is large and a significant contribution from the neck and the wall regions is visible. In addition, about a quarter of the losses occurs in the exterior domain, near the entrance of the holes. This highlights the presence of a jet in the linear regime when considering micro perforation. Despite the fact that the Helmholtz approach is not modeling this effect, it so happens that, for this configuration, it provides correct predictions of the impedance.

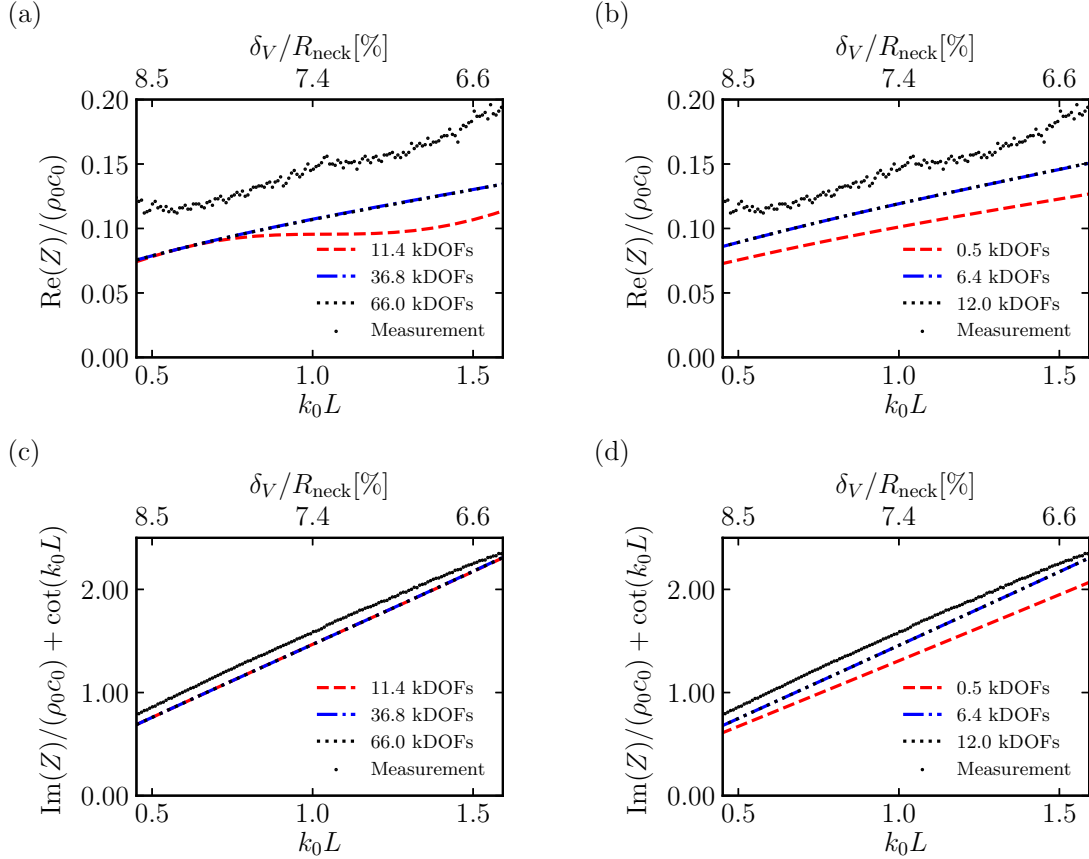


Figure 8: (a), (c) Measured normalized resistance and normalized plate reactance compared with the LNSE model for different numbers of DOF. (b), (d) Measured normalized resistance and normalized plate reactance compared with the Helmholtz model for different numbers of DOF.

6 Convergence of the numerical models

The convergence of the numerical models is investigated in this section. In a first stage, we compare the results obtained from impedance tube measurements to computations performed with different numbers of degrees of freedom (DOF) using the macro-perforated configuration 1.

Good convergence of the LNSE model is already obtained with 36.8 kDOFs (Figure 8(a)). This corresponds to elements of size $0.25R_{\text{neck}}$ on the axis and $0.032R_{\text{neck}}$ on the surface of the neck. In fact, the normalized plate reactance in Figure 8(c) has already converged for a very coarse model with just 11.4 kDOFs. Figures 8(b) and (d) show that the Helmholtz model converges for a number of DOF near 6400. This corresponds to elements of size $0.61R_{\text{neck}}$ on the axis and $0.08R_{\text{neck}}$ on the surface of the neck. This much smaller model size is explained by the facts that (i) the Helmholtz equation is a scalar model while the LNSE involves 4 unknown fields, and (ii) there is no need to resolve the boundary layer with the Helmholtz model.

The accuracy of the models is now investigated by computing the impedance at the resonance frequency of configuration 1. A reference value Z_{ref} for the impedance is defined as the averaged

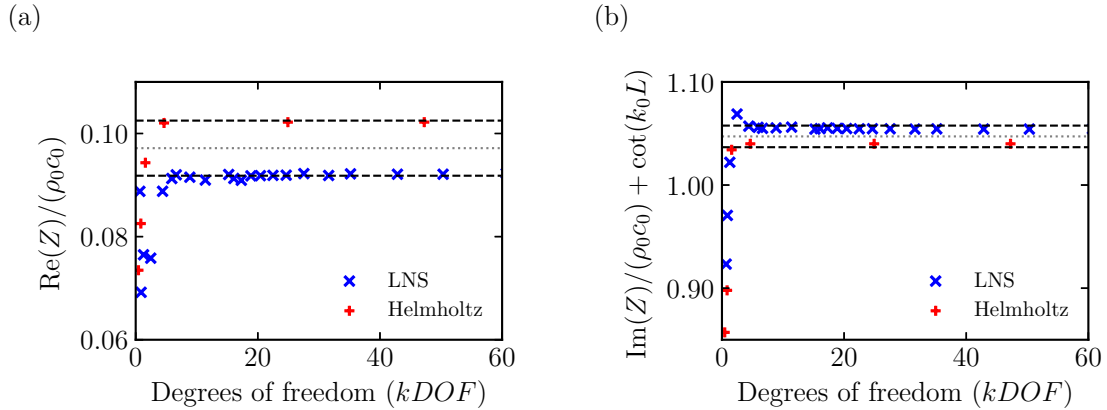


Figure 9: (a) Resistance and (b) plate reactance predicted for configuration 1 as a function of the number of degrees of freedom ($Re_a = 148611$, $Pr = 0.707$). The dotted lines show the reference normalized resistance and the reference normalized plate reactance. The dashed lines show the limits within which the models are considered to be converged, between $+5.5\%$ and -5.5% for the resistance and between $+1.0\%$ and -1.0% for the reactance.

prediction between the Helmholtz model and the LNSE model:

$$Z_{\text{ref}} = \frac{Z_{\text{H}} + Z_{\text{LNSE}}}{2}, \quad (21)$$

in which Z_{H} and Z_{LNSE} are the converged values obtained with the two models.

We assess the convergence of the numerical models by comparing this reference value with the predictions obtained for different numbers of degrees of freedom. Based on the analysis of these predictions, it was found that the models can be considered to be converged when the resistance remains within $+5.5\%$ and -5.5% of the reference resistance $\text{Re}(Z_{\text{ref}})$ and when the reactance remains within $+1.0\%$ and -1.0% of the reference reactance $\text{Im}(Z_{\text{ref}})$. This is shown in Figure 9. The linearized Navier–Stokes model appears to converge for 35 kDOF approximately while the Helmholtz model appears to converge for lower number of DOF, around 5 kDOF. This illustrates that it is much cheaper to solve the Helmholtz equation with a visco-thermal boundary condition than it is to solve the linearized Navier–Stokes equations.

7 Conclusion

Two computational models were considered to predict the acoustic impedance of perforated plates in the linear regime. Both macro- and micro-perforated configurations were considered and detailed comparisons with measured data from an impedance tube were used for validation.

The model based on the linearized Navier–Stokes equations is particularly expensive to solve, but it provides a more detailed and complete picture of the absorption mechanisms. It was used to calculate the viscous dissipation rate for a single hole. It was observed that the overall distribution of dissipation is very different between the macro- and micro-perforated cases. There is also a significant amount of dissipation taking place at the corners of the hole. This contribution to the acoustic absorption is not included in any impedance models and could be of interest to explore further. It is also shown that, in the micro-perforated case, an important contribution to the viscous dissipation comes from outside the hole, illustrating the importance of the end correction used in impedance models to account for this portion of the losses.

The second model to be considered is based on the Helmholtz equation combined with a boundary condition developed by Berggren et al. (2018) which account for the visco-thermal

losses in the acoustic boundary layer. This model is much cheaper to solve compared to the LNSE since it is a scalar model and does not require to resolve the boundary layer in the finite element mesh.

From the comparison with experimental data, both models appear to predict accurately the impedance. The Helmholtz model is well-suited for the macro-perforated case where most of the losses occur along walls of the perforation. For the micro-perforated cases considered in this paper the Helmholtz model also provides good prediction, but a caveat is that the visco-thermal boundary condition cannot account for the losses occurring away from the walls.

A LNSE dispersion relation and plane wave derivations

On the upper boundary Γ_{in} of the computation domain, an incoming plane wave of the form $e^{+i\omega t + ikz}$ is generated by using the following Robin boundary condition:

$$\nabla p' \cdot \mathbf{n} + ikp' = 2ikW e^{ikL_Z} \text{ on } \Gamma_{in}, \quad (22)$$

where $L_Z = L + h + L_T$ and W is the amplitude of the plane wave. The wavenumber k remains to be determined together with the associated expression for the other variables of the linearized Navier–Stokes equations. To that end we use the fact that these variables are also of the form $e^{+i\omega t - ikz}$ to modify equations (6), (7) and (8) and write:

$$\rho' = -\frac{k}{\omega} \mathbf{u}' \cdot \mathbf{n}, \quad p' = -\frac{\alpha}{k} \mathbf{u}' \cdot \mathbf{n}, \quad T' = -\frac{k}{\beta} \mathbf{u}' \cdot \mathbf{n}, \quad p' = [(\gamma - 1)T' + \rho']/\gamma, \quad (23)$$

with

$$\alpha = \omega - ik^2 \frac{\mu_B + \frac{4}{3}}{Re_a}, \quad \beta = \omega - ik^2 \frac{\gamma}{Re_a Pr}.$$

From these relations, and assuming that thermal effects are small ($Pr \rightarrow \infty$), one can recover the definition of the wavenumber (10). One can also obtain the boundary conditions for the linearized Navier–Stokes equations corresponding to an incoming plane wave:

$$\nabla \rho' \cdot \mathbf{n} + ik\rho' = \frac{2k^3}{\omega\alpha} iW e^{ikL_Z}, \quad (24)$$

$$\nabla (\mathbf{u}' \cdot \mathbf{n}) \cdot \mathbf{n} + ik\mathbf{u}' \cdot \mathbf{n} = \frac{-2k^2}{\alpha} iW e^{ikL_Z}, \quad (25)$$

$$\nabla T' \cdot \mathbf{n} + ikT' = \frac{2k^3}{\alpha\beta} iW e^{ikL_Z}. \quad (26)$$

These expressions are used below in the variational formulation of the LNSE.

B LNSE weak formulations

B.1 Mass equation

The weak formulation of the mass conservation equation is

$$\int_{\Omega} q \frac{\partial \rho'}{\partial t} d\Omega = \int_{\Omega} \mathbf{u}' \cdot \nabla q d\Omega - \int_{\Gamma} q \mathbf{u}' \cdot \mathbf{n} d\Gamma, \quad (27)$$

where q is a test function. Incorporating the plane-wave boundary condition (25) in equation (27) yields

$$\int_{\Omega} q \frac{\partial \rho'}{\partial t} d\Omega = \int_{\Omega} \mathbf{u}' \cdot \nabla q d\Omega + \frac{1}{ik} \int_{\Gamma_{in}} q (\mathbf{n} \cdot \nabla) (\mathbf{u}' \cdot \mathbf{n}) d\Gamma + \frac{2k}{\alpha} W e^{ikL_Z} \int_{\Gamma_{in}} q d\Gamma. \quad (28)$$

B.2 Momentum equation

The boundary including the axis and the free-slip boundaries is written $\Gamma_s = \Gamma_{\text{axis}} \cup \Gamma_{\text{ext,lat}} \cup \Gamma_{\text{cav,lat}}$. The weak formulation of the momentum equation reads

$$\begin{aligned} \int_{\Omega} \mathbf{v} \cdot \frac{\partial \mathbf{u}}{\partial t} d\Omega &= \frac{1}{\gamma} \int_{\Omega} (\nabla \cdot \mathbf{v}) [(\gamma - 1)T' + \rho'] d\Omega \\ &- \frac{1}{Re_a} \int_{\Omega} \nabla \mathbf{v} : \left[\nabla \mathbf{u}' + (\nabla \mathbf{u}')^T \right] + (\mu_B - \frac{2}{3}) (\nabla \cdot \mathbf{v}) (\nabla \cdot \mathbf{u}') d\Omega \\ &- \frac{1}{\gamma} \int_{\Gamma} (\mathbf{v} \cdot \mathbf{n}) [(\gamma - 1)T' + \rho'] d\Gamma \\ &+ \frac{1}{Re_a} \int_{\Gamma} \mathbf{v} \cdot \left[\nabla \mathbf{u}' + (\nabla \mathbf{u}')^T \right] \mathbf{n} + (\mu_B - \frac{2}{3}) \mathbf{v} \cdot \mathbf{n} (\nabla \cdot \mathbf{u}') d\Gamma \end{aligned} \quad (29)$$

where \mathbf{v} is a test function. Using the boundary conditions (24) to (26), we find

$$\begin{aligned} \rho_0 \int_{\Omega} \mathbf{v} \cdot \frac{\partial \mathbf{u}}{\partial t} d\Omega &= \frac{1}{\gamma} \int_{\Omega} (\nabla \cdot \mathbf{v}) [(\gamma - 1)T' + \rho'] d\Omega \\ &- \frac{1}{Re_a} \int_{\Omega} \nabla \mathbf{v} : \left[\nabla \mathbf{u}' + (\nabla \mathbf{u}')^T \right] + (\mu_B - \frac{2}{3}) (\nabla \cdot \mathbf{v}) (\nabla \cdot \mathbf{u}') d\Omega \\ &+ \frac{1}{i\gamma k} \int_{\Gamma_{\text{in}}} (\mathbf{v} \cdot \mathbf{n}) (\mathbf{n} \cdot \nabla) [(\gamma - 1)T' + \rho'] d\Gamma \\ &- \left(2W e^{ikLz} - \frac{2W ik^2 e^{ikLz}}{\alpha} \frac{\mu_B + \frac{4}{3}}{Re_a} \right) \int_{\Gamma_{\text{in}}} \mathbf{v} \cdot \mathbf{n} d\Gamma \\ &- ik \frac{\mu_B + \frac{4}{3}}{Re_a} \int_{\Gamma_{\text{in}}} (\mathbf{v} \cdot \mathbf{n}) (\mathbf{u}' \cdot \mathbf{n}) d\Gamma. \end{aligned} \quad (30)$$

B.3 Energy equation

The weak formulation of the energy equation corresponds to

$$\int_{\Omega} \epsilon \frac{\partial T'}{\partial t} d\Omega = - \int_{\Omega} (\nabla \cdot \mathbf{u}') \epsilon - \frac{\gamma}{Re_a Pr} \nabla \epsilon \cdot \nabla T' d\Omega + \frac{\gamma}{Re_a Pr} \int_{\Gamma} \epsilon \nabla T' \cdot \mathbf{n} d\Gamma,$$

where ϵ is a test function. Replacing $\nabla T' \cdot \mathbf{n}$ by the plane-wave boundary condition (26) on Γ_{in} , the weak formulation become

$$\begin{aligned} \int_{\Omega} \epsilon \frac{\partial T'}{\partial t} d\Omega &= - \int_{\Omega} (\nabla \cdot \mathbf{u}') \epsilon - \frac{\gamma}{Re_a Pr} \nabla \epsilon \cdot \nabla T' d\Omega \\ &- ik \frac{\gamma}{Re_a Pr} \int_{\Gamma_{\text{in}}} \epsilon T' d\Gamma \\ &+ \frac{2W ik^3 e^{ikLz}}{\alpha \beta} \frac{\gamma}{Re_a Pr} \int_{\Gamma_{\text{in}}} \epsilon d\Gamma. \end{aligned} \quad (31)$$

C Weak formulation of the Helmholtz model

The variational formulation for the Helmholtz equation is as follows:

$$- \int_{\Omega} \nabla p \cdot \nabla \eta d\Omega + \int_{\Gamma} \nabla p \cdot \mathbf{n} \eta d\Gamma + \omega^2 \int_{\Omega} p \eta d\Omega = 0, \quad (32)$$

where η is a test function.

An incoming plane wave is implemented on the upper boundary of the domain:

$$\frac{\partial p}{\partial n} + i\omega p = 2Wie^{i\omega Lz} \text{ on } \Gamma_{\text{in}} . \quad (33)$$

The boundary condition (18) is implemented on Γ_w .

These boundary conditions are introduced in (32) to give

$$\begin{aligned} \int_{\Omega} -\nabla p \cdot \nabla \eta + \omega^2 p \eta \, d\Omega + \int_{\Gamma_w} -\delta_V \frac{i-1}{2} \nabla_T p \cdot \nabla_T \eta - \delta_T \omega^2 \frac{(i-1)(\gamma-1)}{2} p \eta \, d\Gamma_w \\ + \int_{\Gamma_{\text{in}}} -i\omega p \eta + 2i\omega e^{i\omega Lz} \eta \, d\Gamma_{\text{in}} = 0. \end{aligned} \quad (34)$$

References

- Berggren, M., Bernland, A., and Noreland, D. (2018). Acoustic boundary layers as boundary conditions. *Journal of Computational Physics*, 371:633–650.
- Geuzaine, C. and Remacle, J.-F. (2009). Gmsh: a three-dimensional finite element mesh generator with built-in pre- and post-processing facilities. *International Journal for Numerical Methods in Engineering*, 79(11):1309–1331.
- Guess, A. W. (1975). Calculation of perforated plate liner parameters from specified acoustic resistance and reactance. *Journal of Sound and Vibration*, 40(1):119–137.
- Honzík, P., Durand, S., Joly, N., and Bruneau, M. (2013). On the Acoustic Transfer Function of Slowly Tapered Small Horns Filled With Thermo-Viscous Fluid. *Acta Acustica united with Acustica*, 99(5):694–702.
- Joly, N., Bruneau, M., and Bossart, R. (2006). Coupled Equations for Particle Velocity and Temperature Variation as the Fundamental Formulation of Linear Acoustics in Thermo-Viscous Fluids at Rest. *ACTA ACUSTICA UNITED WITH ACUSTICA*, 92:8.
- Keefe, D. H. (1984). Acoustical wave propagation in cylindrical ducts: Transmission line parameter approximations for isothermal and nonisothermal boundary conditions. *The Journal of the Acoustical Society of America*, 75(1):58–62.
- Laurens, S., Tordeux, S., Bendali, A., Fares, M., and Kotiuga, P. (2013). Lower and upper bounds for the Rayleigh conductivity of a perforated plate. *ESAIM: Mathematical Modelling and Numerical Analysis*, 47(6):1691–1712.
- Maa, D.-Y. (1998). Potential of microperforated panel absorber. *the Journal of the Acoustical Society of America*, 104(5):2861–2866.
- Mbailassem, F., Gourdon, E., Leclère, Q., Redon, E., and Cambonie, T. (2019). Sound absorption prediction of linear damped acoustic resonators using a lightweight hybrid model. *Applied Acoustics*, 150:14–26.
- Renard, Y. and Pommier, J. (2017). GetFEM++. An Open Source Finite Element Library.
- Roberts, D. (1977). Equivalent sand-grain roughness of perforated plate acoustic linings. In *15th Aerospace Sciences Meeting*, Los Angeles, CA, U.S.A. American Institute of Aeronautics and Astronautics.
- Zwikker, C. and Kosten, C. W. (1949). *Sound absorbing materials*. Elsevier, New York.